NJC

PAPER

View Article Online
View Journal

Cite this: DOI: 10.1039/d5nj01918d

Construction of a ZnO/Ag_2O S-type heterojunction and its efficient production of H_2O_2 through piezoelectric catalytic dual reaction pathways†

Jia Tang,[a] Yuanwen Hou,[a] Yuetian Yang,[a] Hongquan Fu,[a] Juan Zhang,[a] Hejun Gao,[ab] Jinming Chang[a] and Yunwen Liao*[ab]

Hydrogen peroxide (H_2O_2) is a crucial industrial chemical with diverse applications, ranging from disinfection and bleaching to chemical synthesis and environmental remediation. However, conventional H_2O_2 production methods, such as the anthraquinone oxidation process, face significant challenges, including high energy consumption, environmental concerns, and reliance on hazardous chemicals. To address these issues, there is a growing need for the development of stable, green, and efficient production technologies. Piezoelectric catalysis has emerged as a cutting-edge solution, leveraging piezoelectric materials to convert mechanical energy into chemical energy. This process facilitates the charge separation necessary for redox reactions, offering a promising pathway for the clean and sustainable production of H_2O_2. In this study, S-type ZnO/Ag_2O heterojunctions were synthesized using a precipitation method. This heterojunction demonstrated exceptional catalytic performance, achieving an impressive H_2O_2 production rate of 346.9 μmol g^{-1} h^{-1}, surpassing many existing catalysts. A key breakthrough of this research lies in the dual reaction pathway mechanism of H_2O_2 production. Unlike traditional methods that rely on a single reaction pathway, the ZnO/Ag_2O catalyst enables simultaneous H_2O_2 generation through both the water oxidation reaction (WOR) and the oxygen reduction reaction (ORR). This dual reaction pathway approach significantly enhances the overall yield. This study not only highlights the potential of piezoelectric catalysis as a high-performance method for H_2O_2 synthesis but also paves the way for further advancements in clean and sustainable chemical production.

Received 7th May 2025,
Accepted 10th July 2025

DOI: 10.1039/d5nj01918d

rsc.li/njc

1. Introduction

Hydrogen peroxide (H_2O_2) is a remarkable chemical compound known for its excellent properties, including zero emissions, strong redox capability, and renewability. Since the 20th century, it has become an indispensable chemical with widespread applications across various fields, such as environmental remediation, chemical manufacturing, biological research, and medical treatments. Its versatility and eco-friendly nature make it a preferred choice for numerous industrial and scientific processes.[1–4] Currently, the anthraquinone method is the primary industrial process for synthesizing hydrogen peroxide (H_2O_2). While this method has been widely adopted due to its ability to produce H_2O_2 on a large scale, it suffers from several significant drawbacks that limit its sustainability and efficiency.[5–7] In light of the limitations of the traditional anthraquinone method—such as its high risk, cost, energy consumption, and environmental impact—researchers have been actively exploring green, low-energy, and scalable alternatives for hydrogen peroxide (H_2O_2) production. As an emerging technology, photocatalysis has attracted considerable interest due to its ability to harness solar energy, a clean and inexhaustible resource, to drive chemical processes. However, despite its promise, photocatalysis faces several challenges that hinder its practical application, such as low light utilization efficiency, poor electron–hole separation and limited application effectiveness.[8,9]

Piezoelectric materials, first discovered by Curie brothers in 1880, have revolutionized the field of energy conversion with their unique ability to transform mechanical energy into electrical energy. This phenomenon arises from their non-centrosymmetric crystal structures, which allow them to generate an electric charge in response to applying mechanical stress. Over the years, piezoelectric materials have found

---

[a] Chemical Synthesis and Pollution Control Key Laboratory of Sichuan Province, College of Chemistry and Chemical Engineering, China West Normal University, Nanchong, Sichuan 637000, China. E-mail: liao-yw@163.com

[b] Institute of Applied Chemistry, China West Normal University, Nanchong, Sichuan 637000, China

† Electronic supplementary information (ESI) available. See DOI: https://doi.org/10.1039/d5nj01918d

widespread applications in sensors, actuators, energy harvesters, and, more recently, in catalytic processes.[8] Some of the most well-known piezoelectric materials include ZnO, $BaTiO_3$, and $PbTiO_3$.[9,10] When external mechanical energy is applied to a piezoelectric material, the material undergoes deformation, causing the positive and negative charge centers within its crystal lattice to shift in opposite directions. This displacement creates a built-in electric field across the material, a phenomenon known as the piezoelectric effect. This electric field can drive the separation of charge carriers (electrons and holes), which are then available to participate in redox reactions on the material's surface.[11] In recent years, piezocatalysis has emerged as a groundbreaking catalytic technology, offering an efficient way to harness mechanical energy from natural sources such as ultrasonic waves, vortex-induced shear, stirring, and physical bending. By harnessing the intrinsic piezoelectric properties of specific materials, piezocatalysis facilitates the direct conversion of mechanical energy into chemical energy, thereby driving redox reactions. This innovative approach has garnered significant attention as a green and sustainable alternative to traditional catalytic methods.[12] The production of hydrogen peroxide (H_2O_2) through catalytic processes often relies on two key reactions: the oxygen reduction reaction (ORR) and the water oxidation reaction (WOR). Both mechanisms have their unique advantages and limitations, but the WOR is increasingly being recognized as a more rational and efficient approach for H_2O_2 production, particularly due to its ability to overcome the limitations associated with the ORR.[13,14] Indeed, growing interest in developing dual reaction pathway catalysts capable of producing hydrogen peroxide (H_2O_2) through both the water oxidation reaction (WOR) and the oxygen reduction reaction (ORR) reflects a significant shift toward more efficient and versatile catalytic systems.

ZnO is a highly versatile and widely studied material, particularly in the field of catalysis, due to its unique properties and advantages. As a wide-bandgap n-type semiconductor with a bandgap of 3.37 eV, ZnO has garnered significant attention for its potential in various applications, including photocatalysis, piezocatalysis, and sensing.[15,16] The wide bandgap (3.37 eV) of ZnO, while beneficial for certain applications, poses a significant challenge due to its low efficiency in electron–hole separation and limited visible light absorption. These limitations hinder its widespread industrial use, particularly in photocatalytic and piezocatalytic processes. To overcome these limitations, constructing ZnO-based heterojunctions with complementary semiconductors (*e.g.*, Ag_2O) has emerged as a highly effective strategy. Ag_2O, a p-type narrow bandgap semiconductor with a bandgap of approximately 1.3 eV, complements ZnO's properties and significantly enhances its catalytic performance.[17] The design of heterojunctions plays a critical role in determining the efficiency of catalytic systems, particularly in balancing charge separation and redox capacity. Traditional type I and type II heterojunctions, while effective in enhancing charge separation, often come with trade-offs that can reduce the redox potential of the system. This limitation has led to the exploration of alternative heterojunction designs, such as S-scheme heterojunctions, which offer a more effective way to improve both charge separation and redox capacity.[18–24]

In this study, we synthesized an S-type ZnO/Ag_2O heterojunction using a precipitation method. A key distinction between our approach and the typical single reaction pathway method for generating H_2O_2 lies in the significant enhancement of catalytic efficiency achieved through the use of double reaction pathway H_2O_2 generation process. Furthermore, to assess the piezoelectric catalytic performance of the ZnO/Ag_2O heterojunction, we employed the iodine assay as a reliable measurement technique. Then, capture experiments were conducted to elucidate the mechanism of H_2O_2 production by the heterojunction. In addition, the successful synthesis of an S-type heterojunction was verified by *in situ* XPS technology. Ultimately, the piezoelectric stability and reusability of the catalyst were evaluated, highlighting its promising potential for practical applications and further development.

2. Experimental methods

2.1. Chemicals

Zinc sulfate heptahydrate ($ZnSO_4{\cdot}7H_2O$) was provided by Shandong West Asia Chemical Co., Ltd, dodecyl sulfate (SDBS, $CH_3(CH_2)_{11}O$-SO_3Na) was purchased from Shanghai Aladdin Co., Ltd in China, sodium hydroxide (NaOH) was obtained from Shanghai Titan Technology Co., Ltd, and silver nitrate ($AgNO_3$) was obtained from Shanghai Sinopharm Chemical Reagent Co., Ltd. All chemistries are analytically pure grade and require no further purification.

2.2. Preparation of piezoelectric materials

The composite materials were synthesized *via* a precipitation method. Initially, 2.7 g of $ZnSO_4{\cdot}7H_2O$, 3.4 g of $AgNO_3$, 1.6 g of NaOH, and 480 mg of SDBS (with SDBS mass consistently maintained at 30% of NaOH) were dissolved in 150 mL of deionized water under vigorous stirring until complete dissolution was achieved. Subsequently, the reaction temperature was elevated to 80 °C and held constant for 2.5 hours. Post-reaction, the mixture underwent a washing process involving three cycles of deionized water and anhydrous ethanol, followed by centrifugation for product recovery. The final product was then dried at 60 °C for 12 hours, yielding a ZnO/Ag_2O composite with a molar ratio of 1 : 1. For comparative analysis, the quantities of $ZnSO_4{\cdot}7H_2O$ and $AgNO_3$ in the initial reactants were systematically varied to fabricate ZnO/Ag_2O composite heterojunctions with different molar ratios.[25]

2.3. Characterization

X-ray diffraction (XRD, TD-3500, Dandong Tongda) was used to analyze the phase and crystal structure of the catalyst. The morphology, particle size and chemical composition of the products were detected by scanning electron microscopy (SEM, ZEISS Gemini-500, Germany) and transmission electron microscopy (TEM, Thermo Fisher 2000, USA). X-ray photoelectron spectroscopy (XPS, Thermo Fisher Scientific KAlpha, USA) was used to analyze the chemical state of the elements on the surface of the catalyst. The binding energy of the elements was calibrated using C1s (284.8 eV) as the benchmark. Catalyst molecules were detected and characterized at 400–4000 cm^{-1} after mixing with KBr using a Thermo Fisher Technology infrared spectrometer (FTIR, NICO-LET6700, Thermo Fisher Technology, USA). The UV-Vis absorption spectra of the catalyst in the wavelength range of 200–800 nm were determined using UV-vis DRS and UV-2600 (Shimadzu, Japan) against the background of $BaSO_4$. Piezoelectric properties are measured by piezoelectric responsive force microscopy (PFM, Bruker Dimension Icon, Germany).

2.4. Performance test of catalyst hydrogen peroxide production

100 mg of the catalyst was placed in a brown stoppered conical flask, followed by the addition of 45 mL of ultrapure water and 5 mL of a sacrificial agent (methanol, ethanol, or isopropanol). The mixture was subjected to ultrasonication in an ultrasonic machine (400 W, 40 kHz). Samples were collected every 30 minutes, and 3.5 mL of the solution was withdrawn and filtered. The hydrogen peroxide (H_2O_2) content in the filtered supernatant was determined using an iodine assay. Specifically, 200 μL of the supernatant was mixed with 50 μL of 0.01 M ammonium molybdate solution ($(NH_4)_2MoO_4$) and 2 mL of 0.1 M potassium iodide (KI) solution. The resulting mixture was analyzed using a UV-Vis spectrophotometer at a wavelength of 352 nm.

3. Results and discussion

3.1. Structural characterization

The crystal structure of the composites with different proportions was analyzed using X-ray diffraction (XRD), as shown in Fig. 1 The diffraction peaks observed at 2θ values of 31.76°, 34.42°, 36.25°, 47.53°, 56.6°, 62.86°, 67.96°, and 69.09° correspond to the (100), (002), (101), (102), (112), and (201) crystal planes of hexagonal ZnO (PDF# 36-1451), respectively. Additionally, the peaks observed at 32.79°, 38.04°, 47.06°, and 54.9° are attributed to the (111), (200), (211), and (220) planes of cubic phase Ag_2O (PDF# 43-0997). These results confirm that the prepared composite consists of both hexagonal ZnO and cubic Ag_2O. The narrow and intense diffraction peaks indicate that the synthesized sample exhibits high crystallinity. Notably, no peaks corresponding to impurities or unreacted metal species were detected, further confirming that the nanocomposites are primarily composed of ZnO and Ag_2O. Based on these findings, it can be preliminarily concluded that the composite heterojunction was successfully synthesized.

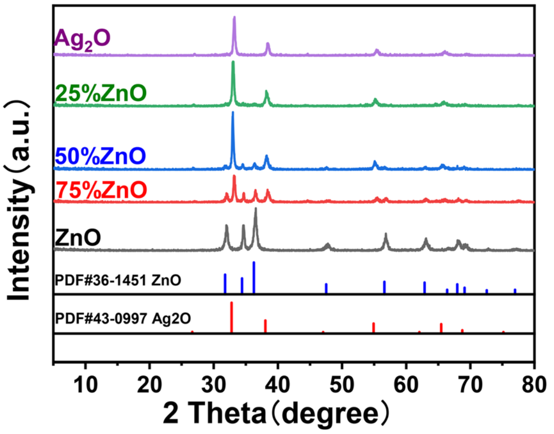

Fig. 1 XRD patterns of complexes with different ZnO and Ag_2O contents.

To further confirm the formation of heterojunctions, the samples were characterized using scanning electron microscopy (SEM). Fig. 2(a) and (c) presents the SEM images of pure ZnO, 50% ZnO composite, and pure Ag_2O, respectively. As shown in the SEM images, pure ZnO exhibits a densely arranged structure of anisotropic ZnO nanosheets, while pure Ag_2O displays an irregular nanospherical morphology. In the 50% ZnO heterojunction composite, the dense Ag_2O spheres are embedded within the ZnO nanosheets. The synthesis method employed in this study resulted in a roughened surface of ZnO, which increases the number of active sites and enhances the piezoelectric catalytic efficiency. These observations provide clear evidence for the successful synthesis of the heterojunction structure.

The morphological characteristics of the synthesized ZnO/Ag_2O heterostructure were further examined using transmission electron microscopy (TEM). Fig. 2(d) and (e) displays typical TEM images of the prepared heterostructure, highlighting the lattice fringes of the nanostructure. The lattice fringes with interplanar spacings of 0.236 nm, 0.192 nm, and 0.258 nm correspond to the (200), (211), and (002) crystal planes of Ag_2O nanosheets, respectively. Additionally, at the interface between the two components, a clear continuity in the lattice fringes is observed, providing strong evidence for the formation of heterojunctions between ZnO and Ag_2O. These findings confirm the successful integration of the two materials into a cohesive heterostructure.[26,27] The TEM images clearly reveal that the spherical Ag_2O particles are adsorbed and embedded within the ZnO nanosheets. These TEM observations are in excellent agreement with the SEM results, further confirming the successful formation of the ZnO/Ag_2O heterostructure and its well-integrated morphology.

X-ray photoelectron spectroscopy (XPS) was employed to analyze the surface composition and chemical states of pure ZnO, pure Ag_2O, and 50% ZnO. The full-scan survey spectrum is presented in Fig. 3(a), which reveals the presence of only O, Zn, and Ag peaks in the 50% ZnO spectrum, with no additional peaks corresponding to other elements. This indicates that the synthesized 50% ZnO product is of high purity. The Zn 2p spectra of the samples are shown in Fig. 3(b). For the 50% ZnO sample, the Zn 2p spectrum can be deconvoluted into two Gaussian peaks centered at 1021.6 eV and 1044.6 eV, respectively. The binding energy separation of 23 eV corresponds to the spin–orbit splitting of the $2p_{3/2}$ and $2p_{1/2}$ components, confirming the presence of Zn in the Zn^{2+} oxidation state, consistent with the ZnO phase. These results further validate the chemical composition and oxidation states of the elements in the synthesized heterostructure.[28] In Fig. 3(d), the Ag 3d spectrum of the composite can be deconvoluted into two peaks centered at 368 eV and 374.1 eV, with a binding energy

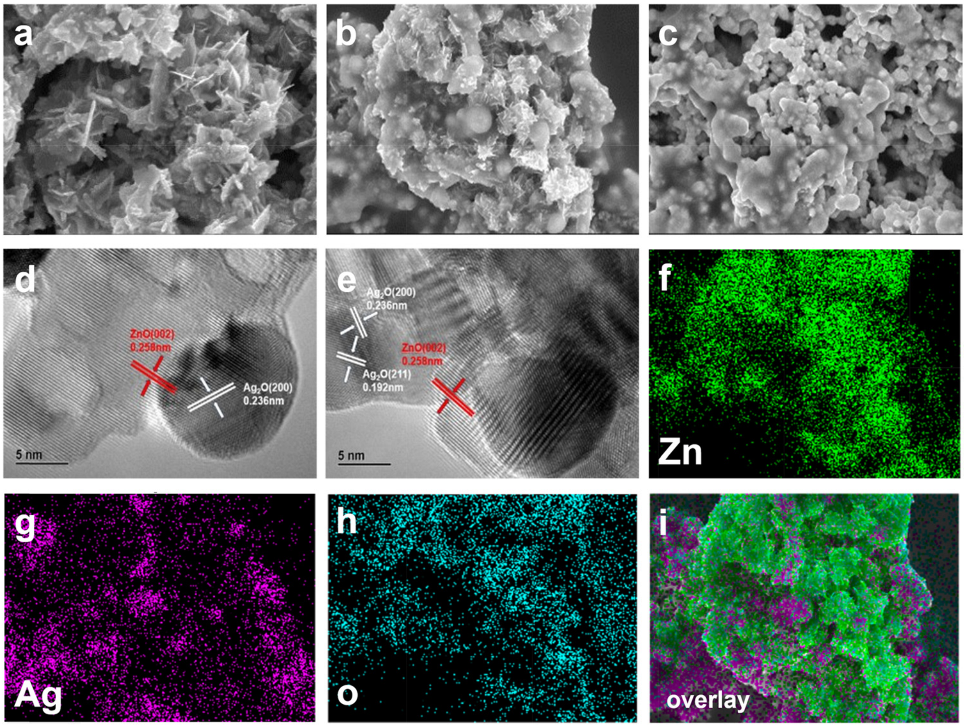

Fig. 2 (a)–(c) SEM images of pure ZnO, 50% ZnO, and pure Ag–O; (d) and (e) TEM image of M50% ZnO; and (f)–(i) mapping of 50% ZnO.

separation of 6 eV. These peaks correspond to Ag $3d_{5/2}$ and Ag $3d_{3/2}$ of metallic silver, respectively, confirming that the Ag element exists in the Ag^+ oxidation state within the Ag_2O phase.[29] This finding is consistent with the XRD and HRTEM results, further supporting the successful preparation of the heterojunction structure. In Fig. 3(c), the O 1s spectrum shows a peak at 530.1 eV, which corresponds to Ag–O and Zn–O bonds, while the other peak at 531.2 eV is attributed to the O–H groups from water molecules adsorbed on the surface of the heterojunction. The XPS spectra also provide insights into charge transfer within the heterojunction. The Zn 2p spectra (Fig. 3(b)) exhibit a positive shift from 1021.4 eV and 1044.5 eV in pure ZnO to 1021.6 eV and 1044.6 eV in the 50% ZnO composite, indicating a decrease in electron density around ZnO. In contrast, the Ag 3d spectra show a slight negative shift from pure Ag_2O to the 50% ZnO composite, suggesting an increase in electron density at the Ag_2O sites. This observation implies that electrons flow from ZnO to Ag_2O during the reaction, driven by the formation of an internal electric field at the interface. This internal electric field balances the Fermi levels of the composite material by directing the movement of electrons, further confirming the effective formation of the heterojunction structure.[18]

Fig. 4 presents the FTIR spectra of the composites with varying proportions of ZnO and Ag_2O, revealing several significant characteristic peaks that further confirm the successful synthesis of the catalyst. In the spectra of pure Ag_2O, 25% ZnO, 50% ZnO, and 75% ZnO, a distinct peak at 704 cm^{-1} is observed, corresponding to the Ag–O stretching vibration. This peak is absent in the spectrum of pure ZnO, consistent with the XRD results, and serves as a fingerprint for the presence of Ag_2O. A characteristic peak at 881 cm^{-1} is present in all five spectra, which may arise from the bending vibration of Zn–O (or Ag–O). For pure ZnO, the broad peaks at 3380 cm^{-1} and 1661 cm^{-1} are attributed to the O–H stretching and bending vibrations, respectively, of water molecules adsorbed on the surface. These observations provide additional evidence for the successful formation of the ZnO/Ag_2O heterostructure and highlight the presence of surface-adsorbed water in the pure ZnO sample.[30] In pure Ag_2O, 25% ZnO, 50% ZnO, and 75% ZnO, the vibration bands at 1367 cm^{-1}, 1447 cm^{-1}, 1661 cm^{-1}, and 3177 cm^{-1} belong to the O–H bending, C–H bending, C–O absorption, and O–H stretching, respectively.[31] These peaks in FTIR spectra typically come from the absorption of CO_2 from water molecules and air.[32] Compared to the FTIR spectra of pure ZnO and pure Ag_2O, the spectra of 25% ZnO, 50% ZnO, and 75% ZnO exhibit mixed characteristic peaks corresponding to both Ag_2O and ZnO. This observation confirms the successful synthesis of the composites, as the presence of distinct vibrational modes from both components demonstrates the coexistence and integration of Ag_2O and ZnO within the heterostructure. These results further validate the formation of the composite materials and highlight the effective combination of the two phases.

Under mechanical stress or strain, polarized positive and negative charges are generated at opposite ends of the crystal.[33] To investigate the piezoelectric properties of the material, piezoelectric force microscopy (PFM) experiments were conducted using 50% ZnO as the target. A non-contact atomic force microscope (AFM) probe was employed to measure the surface

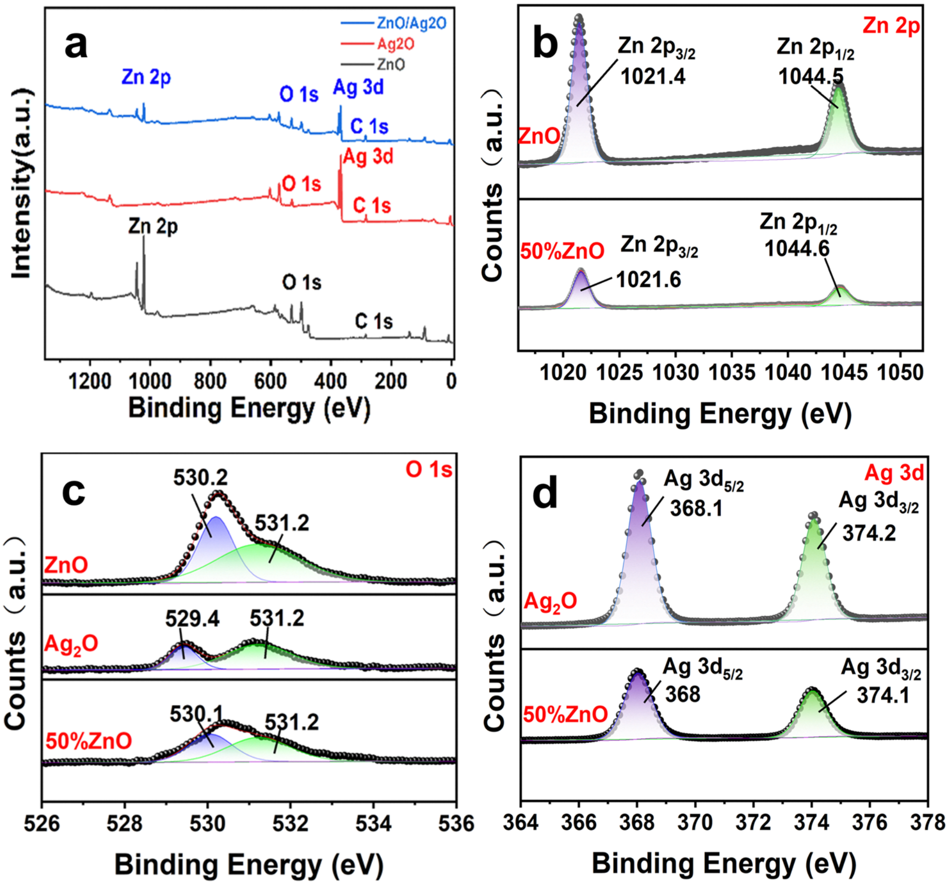

Fig. 3 XPS survey of pure ZnO, 50%ZnO, pure Ag_2O; high resolution XPS spectra of (a) survey scan, (b) Zn 2p, (c) O 1s and (d) Ag 3d.

piezoelectric potential of the material. Fig. 5(b), (c) and (e) presents the PFM morphology, amplitude, and phase images of 50% ZnO within a randomly selected scan area, where the sample height varies in the range of −39.8 to 72.2 nm. When a conductive probe applies a voltage to the catalyst's surface, a distinct contrast is observed in both the amplitude and phase images, confirming the presence of a piezoelectric response in the composite material. These results demonstrate the material's ability to generate piezoelectric effects under external stimuli.[34] The piezoelectric potential of 50% ZnO, as measured by PFM in the dark, reveals a surface potential of approximately 334.3 μV (Fig. 5(c)), highlighting its excellent piezoelectric properties. When an AC voltage of ±12 V is applied to the sample, as shown in Fig. 5(a) and (d), that 50% ZnO exhibits a typical butterfly-shaped amplitude curve and a phase hysteresis loop with a switching angle of 189°. These observations confirm the presence of a local piezoelectric polarization field within the crystalline structure, providing strong evidence for the piezoelectric behavior of the 50% ZnO composite. These results underscore the feasibility of 50% ZnO as an effective piezocatalytic material for applications requiring piezoelectric responses.[35–37]

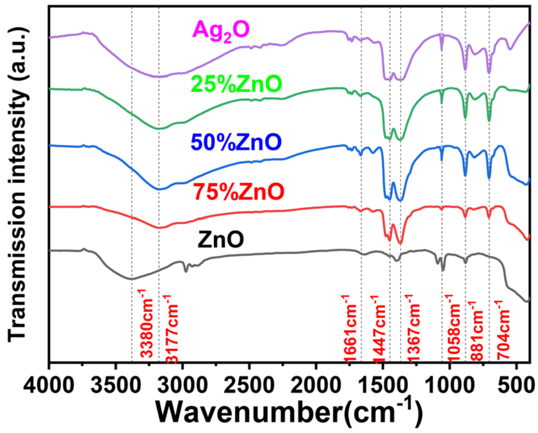

Fig. 4 FTIR analysis of pure ZnO, 75%ZnO, 50%ZnO, 25%ZnO, and pure Ag_2O.

3.2. The performance of piezoelectric catalysis for H_2O_2 production

The catalytic activity was evaluated by measuring the amount of I_3^- produced using the iodometric method, with KI as an indicator, and determining its concentration spectrophotometrically at 352 nm.[38,39] Fig. 6(a) and (c) illustrate the formation of H_2O_2 under different experimental conditions: simultaneous ultrasonication with the addition of the catalyst, addition of the catalyst only, and ultrasonication only. As shown in the figures, the final yield of H_2O_2 is negligible when only ultrasound or the catalyst is used

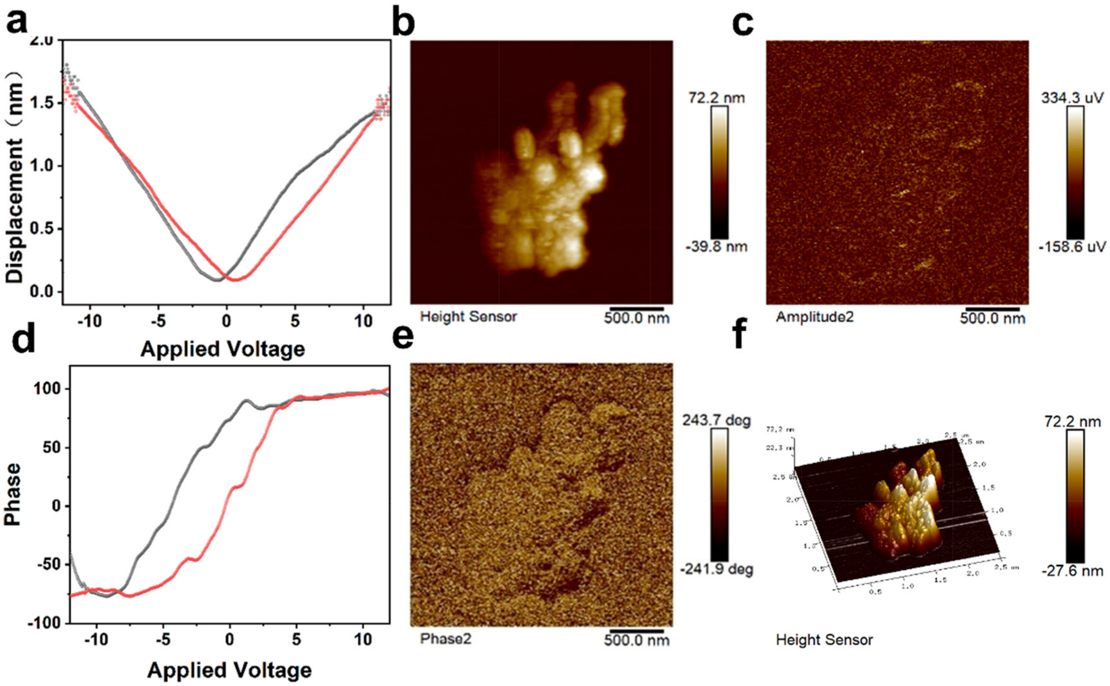

Fig. 5 PFM characterization of 50% ZnO: (a) amplitude–voltage butterfly loop, (b) topography image, (c) piezoelectric potential, (d) phase–voltage hysteresis loop and (e) phase image and (f) 3D image of the distribution of the piezoelectric potential according to the morphology image over 50% ZnO nanoplates.

individually. This observation rules out any potential interference from sonochemistry in this system, confirming that H_2O_2 generation is primarily driven by the piezocatalytic activity of the catalyst under ultrasonication.[7,40] In stark contrast, when both ultrasonication and the piezoelectric catalyst are present, H_2O_2 is produced in significant amounts, and its concentration increases steadily over time. This clearly demonstrates that the generation of H_2O_2 in the piezocatalytic process is the result of the synergistic interaction between ultrasound and the catalyst. The mechanical energy provided by ultrasonication activates the piezoelectric properties of the catalyst, leading to the efficient production of H_2O_2. Thus, it can be concluded that the combined action of ultrasound and the catalyst is essential for the observed piezocatalytic activity.[41,42]

To determine the optimal reaction conditions for the piezocatalytic system, the effects of composite ratio, initial pH, and type of sacrificial agent on the performance of H_2O_2 production were systematically investigated. By varying the molar ratios of $ZnSO_4{\cdot}7H_2O$ and $AgNO_3$ in the raw materials, the influence of different composite proportions on the piezocatalytic properties was studied. The overall trend in Fig. 6(b) and (d) exhibits a volcanic-type relationship. As the ZnO content increases, the H_2O_2 formation rates of pure ZnO, 75% ZnO, 50% ZnO, 25% ZnO, and pure Ag_2O gradually increase, with values of 67.8 μmol g^{-1} h^{-1}, 143.2 μmol g^{-1} h^{-1}, 346.9 μmol g^{-1} h^{-1}, 318.7 μmol g^{-1} h^{-1}, and 164.7 μmol g^{-1} h^{-1}, respectively. The performance peaks when the molar ratio of ZnO to Ag_2O is 1 : 1. Combined with the analysis results of XPS, it can be seen that the electrons (e^-) of ZnO are gradually transferred from the CB to the VB of Ag_2O, and the separation of electrons (e^-) and holes (h^+) is enhanced compared with pure ZnO or pure Ag_2O, while their recombination is effectively suppressed. This optimal balance between ZnO and Ag_2O maximizes the piezocatalytic efficiency, leading to the highest H_2O_2 production rate.[26] However, since Ag_2O tends to trap electrons, when the Ag_2O content exceeds 50% (*i.e.*, when the molar ratio of Ag_2O is higher than 50%), too much Ag_2O may compete for electrons, resulting in some electrons being unable to participate in the reaction, further degrading piezoelectric catalytic performance.[43] This indicates that by optimizing the composite ratio, the piezocatalytic performance can be significantly enhanced compared to that of either individual component alone. The results demonstrate that the ZnO/Ag_2O heterojunction successfully improves the piezoelectric catalytic activity. As shown in Table 1, compared with the catalysts reported in the literature, ZnO has a wide bandgap but high activity and easy regulation, and the catalyst in this study is very competitive under the modification of Ag_2O with a narrow bandgap, highlighting its potential for practical application. These findings highlight the promising prospects of the ZnO/Ag_2O composite as an efficient piezocatalytic material for H_2O_2 production and related applications.

The influence of electron donors on the performance of piezocatalytic H_2O_2 production was investigated using several common sacrificial agents, including methanol (MeOH), ethanol (EtOH), and isopropanol (IPA). Fig. 7(a) and (c) show the yield of H_2O_2 after 3 hours of piezocatalytic reaction using 50% ZnO in aqueous solutions containing different alcohols at the same molar concentration (10%). The H_2O_2 production rates were as follows: methanol (302.4 μmol g^{-1} h^{-1}) > ethanol (170.5 μmol g^{-1} h^{-1}) > isopropanol (167.2 μmol g^{-1} h^{-1}).[49] A review of the literature reveals that the addition of methanol,

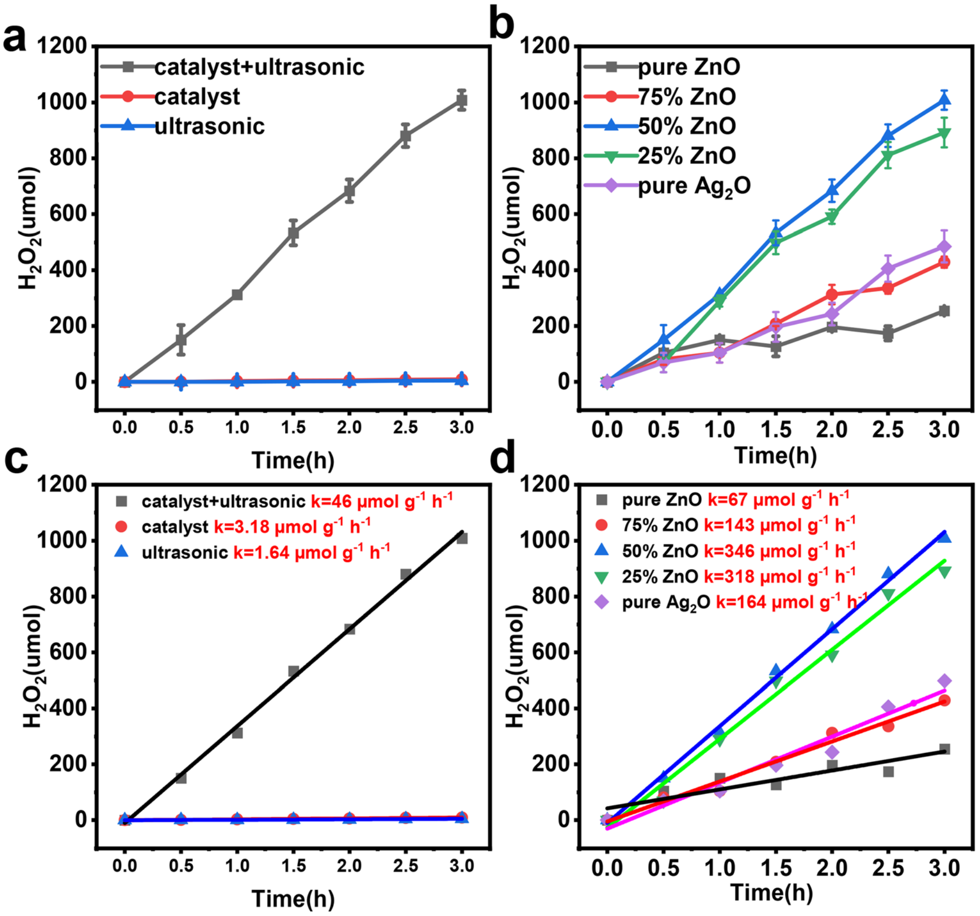

Fig. 6 (a) H_2O_2 production under the catalyst, ultrasonication, and catalyst and ultrasonication; (b) H_2O_2 production at different ZnO and Ag_2O contents; (c) H_2O_2 production rate under the catalyst, ultrasonication, catalyst and ultrasonication; (d) H_2O_2 production rate at different ZnO and Ag_2O contents.

which has a greater electron-donating capacity (electron-donating capacity: methanol > ethanol > isopropanol), results in superior piezocatalytic performance compared to the other two sacrificial agents. This is attributed to methanol's ability to more effectively suppress charge recombination by rapidly donating electrons, thereby enhancing the separation of electron–hole pairs and improving the overall efficiency of the piezocatalytic process. These findings align with the experimental results, further confirming the critical role of sacrificial agents in optimizing piezocatalytic activity.[50]

In addition, the pH value of the aqueous solution can significantly influence the proton-coupled electron transfer process, thereby affecting the formation of H_2O_2. To investigate this, the effect of the initial solution pH on the H_2O_2 yield was explored using methanol as the sacrificial agent and 50% ZnO as the catalyst. As shown in Fig. 7(b) and (d), the efficiency of piezocatalytic H_2O_2 production remained relatively stable at pH = 7, 8, and 9, with no significant changes observed. However, at pH 10, the yield of H_2O_2 decreased dramatically. This decline can be attributed to the fact that H_2O_2 is prone to decomposition in highly alkaline environments, as reported in the literature, leading to a significant reduction in the net production rate of H_2O_2. These results highlight the importance of maintaining an optimal pH range to maximize piezocatalytic performance and H_2O_2 yield.[51]

Table 1 This experiment was compared with the reported performance of piezoelectric catalytic hydrogen peroxide production

Catalyst	H_2O_2 yield (μmol g^{-1} h^{-1})	Ultrasonic power	Ref.
ZnO/Ag_2O	346.9	400 W and 40 kHz	This work
BiOCl	249.7	150 W and 53 kHz	44
$V\text{-}NaNbO_3$	102.6	192 W and 68 kHz	45
$ZnS/In_2S_3/BaTiO_3$	107.9	150 W and 40 kHz	7
$g\text{-}C_3N_4$	68	150 W and 53 kHz	46
$BaTiO_3$	175.71	100 W and 50 kHz	47
$PTFE/RbBiNb_2O_7$	219.2	260 W and 68 kHz	48

The reusability of the piezoelectric catalyst was evaluated through recycling experiments. As shown in Fig. 8(b), after six cycles, the yield of piezocatalytic H_2O_2 remained above 90% of the initial yield, with no significant decline. In addition, the XRD spectra in Fig. 8(a), as well as the IR spectra in Fig. S1 (ESI†), show that the characteristic peaks of the catalyst remain essentially unchanged before and after the reaction. Fig. S2 (ESI†) shows the SEM after the reaction, which can be observed to be almost indistinguishable from before the reaction, confirming the structural stability of the catalyst. Overall, the catalyst exhibits excellent recovery performance and can be

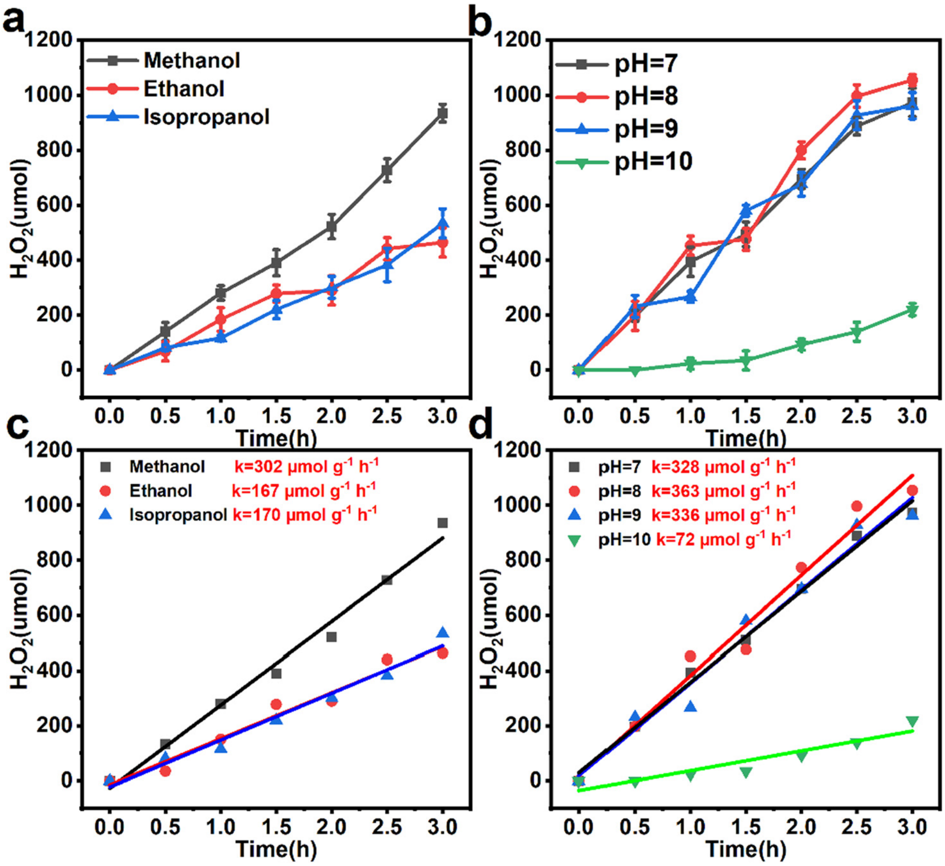

Fig. 7 (a) H_2O_2 production under different sacrificial agents, (b) H_2O_2 production at different pH values, (c) H_2O_2 production rate under different sacrificial agents and (d) H_2O_2 production rate at different pH values.

effectively reused within a reasonable range, demonstrating its potential for practical applications.[52]

3.3. Catalytic mechanism

Fig. 9(a) presents the UV-Vis absorption spectra of heterogeneous structures with varying ZnO/Ag_2O ratios. A noticeable blue shift was observed in the UV-Vis spectra of pure ZnO nanoparticles as the Ag_2O doping ratio increased. Utilizing the Kubelka–Munk method,[53] the bandgap energies of the nanocomposites were determined to be 1.74 eV for pure Ag_2O, 2.98 eV for 25% ZnO, 3.16 eV for 50% ZnO, 3.24 eV for 75% ZnO, and 3.32 eV for pure ZnO, as illustrated in Fig. 9(b). The introduction of Ag_2O nanoparticles resulted in a reduction of the bandgap in ZnO/Ag_2O nanoparticles. Consequently, ZnO/Ag_2O nanocomposites offer enhanced opportunities for electron–hole separation, thereby improving catalytic efficiency.[54] As illustrated in Fig. S3 (ESI†), the 50% ZnO sample exhibits the smallest arc radius in the electrochemical impedance spectroscopy (EIS)

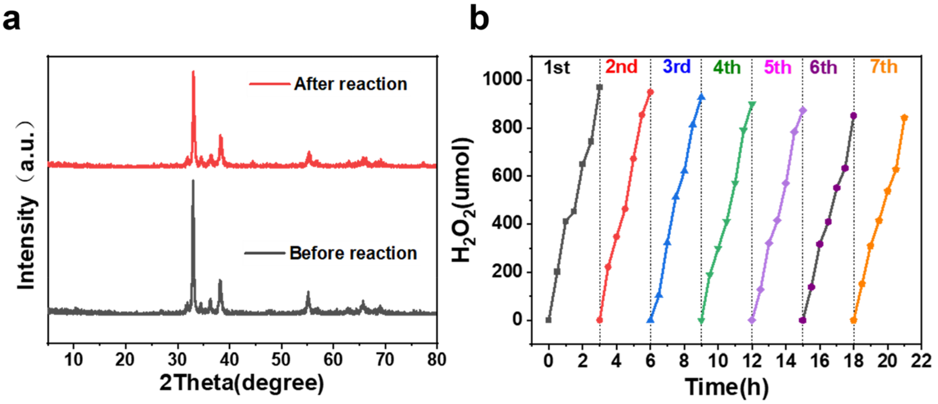

Fig. 8 (a) The XRD patterns after reaction and before reaction; (b) catalytic stability test.

Nyquist plot, demonstrating the most efficient charge transfer kinetics among the tested samples. To further investigate the charge carrier dynamics, photoluminescence (PL) spectroscopy was performed (Fig. S4, ESI†). The 50% ZnO sample shows the lowest PL intensity, indicating its superior charge separation capability and effective suppression of electron–hole pair recombination. These findings provide a plausible explanation for the observed enhancement in hydrogen peroxide production efficiency, where the 50% ZnO sample demonstrated the highest yield.

To further determine the band positions of the catalyst, XPS valence band (XPS-VB) analysis was conducted. The VB potentials of ZnO and Ag_2O were found to be located at 2.21 eV and 0.33 eV, respectively (Fig. 9(c) and (d)). To account for the contact potential difference between the sample and the spectrometer (*vs.* NHE, pH = 7), the actual VB positions were calculated using eqn (1), where Φ (4.38 eV) represents the work function of the XPS analyzer.[55] Therefore, the actual VB potentials of the ZnO and Ag_2O samples are determined to be 2.15 eV and 0.27 eV, respectively. By combining the Zn 2p and Ag 3d spectra from the XPS analysis, it is concluded that electrons flow from ZnO to Ag_2O. This electron transfer behavior supports the formation of an S-type heterojunction between ZnO and Ag_2O. In addition, to verify the successful formation of the S-type heterojunction, we tested *in situ* XPS. As can be seen

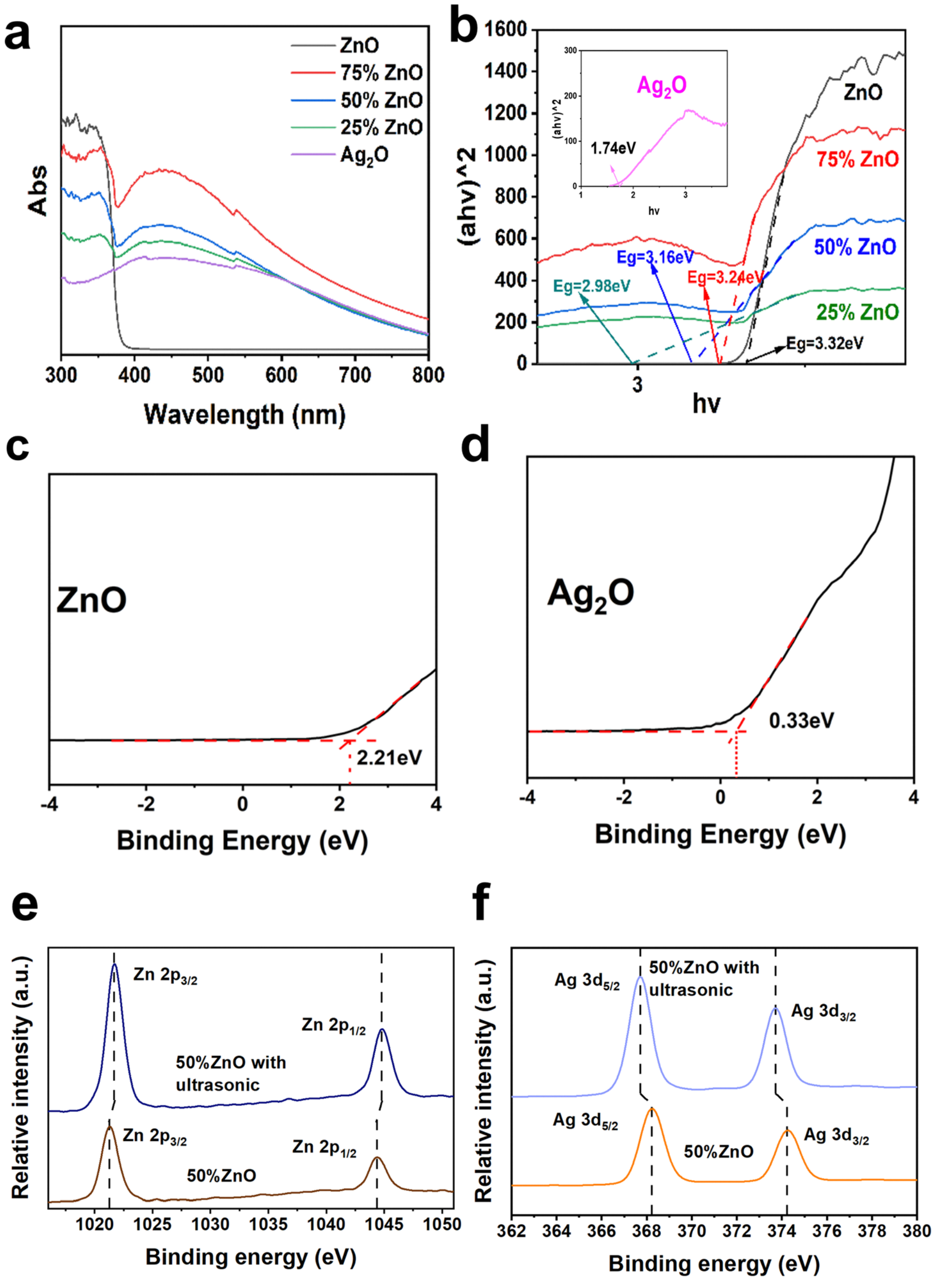

Fig. 9 (a) UV-vis DRS spectra, (b) the corresponding Tauc plot, (c) and (d) XPS valence band spectra of pure Ag_2O and pure ZnO, (e) and (f) *in situ* irradiated XPS spectra of Zn 2p and Ag 3d for 50% ZnO as compared with those for 50% ZnO with ultrasonication.

from Fig. 9(e) and (f), the binding energy of Zn increases and that of Ag decreases when ultrasound is present, indicating that there are electrons flowing from Zn to Ag, which is consistent with the characteristics of the S-type heterojunction.[21–24] As an important prerequisite for the formation of H_2O_2, the standard redox potential plays a critical role in relation to the heterojunction band structure. The band structure of the heterojunction is closely aligned with the standard redox potentials of the oxygen reduction reaction (ORR) and water oxidation reaction (WOR), which are essential for H_2O_2 generation, as illustrated in Fig. 10. As can be seen from the figure, the ORR (indirect: $O_2/{}^{\bullet}O_2^-$, −0.33 V; ${}^{\bullet}O_2^-/H_2O_2$, +1.44 V; direct: O_2/H_2O_2, +0.68 V)[53,56] is corrected over the VB of Ag_2O, and the WOR (indirect: $OH^-/{}^{\bullet}OH$, 1.99 V; direct: H_2O/H_2O_2, +1.76 V) is more negative than the VB of ZnO. Thus, the heterojunction may trigger the ORR ($O_2 \rightarrow {}^{\bullet}O_2^- \rightarrow H_2O_2$) and WOR (direct: $H_2O \rightarrow {}^{\bullet}OH \rightarrow H_2O_2$; indirect: $OH^- \rightarrow {}^{\bullet}OH \rightarrow H_2O_2$) reactions through the accumulation of electrons and holes in the CB of Ag_2O and the VB of ZnO. Indeed, the formation of heterojunctions can shift the generation of H_2O_2 from a conventional single reaction pathway to a more efficient dual reaction pathway. In a single reaction pathway, H_2O_2 production typically relies on either the oxygen reduction reaction (ORR) or the water oxidation reaction (WOR) alone. However, in a dual reaction pathway, both reactions can occur simultaneously, significantly enhancing the overall yield of H_2O_2.

$$\text{EVB } (vs.\ \text{NHE}) = \Phi + \text{EVB (determined by XPS)} - 4.44 \quad (1)$$

To investigate the reaction pathway of H_2O_2 formation, scavenger experiments were conducted using *tert*-butanol (TBA), silver nitrate ($AgNO_3$), L-ascorbic acid (VC), and nitrogen (N_2) as quenchers for hydroxyl radicals (${}^{\bullet}OH$), electrons (e^-), superoxide radicals (${}^{\bullet}O_2^-$), and oxygen (O_2), respectively. As shown in Fig. 11(a), the formation of H_2O_2 is severely inhibited upon the introduction of VC, which acts as a scavenger for superoxide radicals (${}^{\bullet}O_2^-$). This observation confirms that ${}^{\bullet}O_2^-$ is a critical intermediate in the generation of H_2O_2.[57,58] The yield of H_2O_2 was inhibited to 521.62 μmol after continuous N_2 injection, indicating that dissolved oxygen is an essential but not the only source for the synthesis of hydrogen peroxide. Therefore, we consider the oxygen reduction reaction (ORR) to be one of the pathways for the formation of H_2O_2. A series of studies have shown that the ORR pathway can be divided into a two-step single-electron reaction (eqn (2) and (3)) and a direct one-step two-electron reaction (eqn (4)):[53,56]

$$O_2 + e^- \rightarrow {}^{\bullet}O_2^- \quad (2)$$

$$ {}^{\bullet}O_2^- + 2H^+ + e^- \rightarrow H_2O_2 \quad (3)$$

$$O_2 + 2H^+ + 2\,e^- \rightarrow H_2O_2 \quad (4)$$

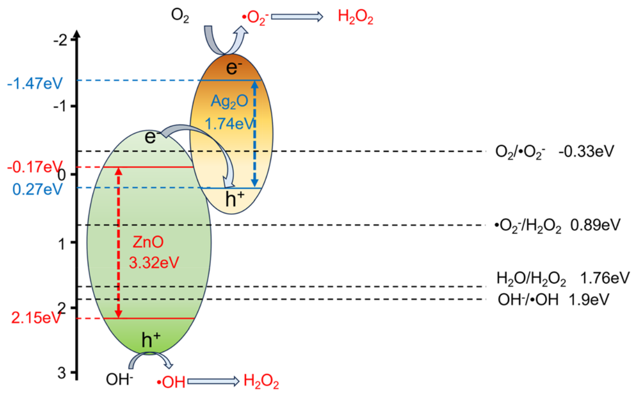

Fig. 10 Schematic illustration of the band structures of the prepared samples.

To investigate the reaction pathway of the oxygen reduction reaction (ORR), we employed DMPO spin-trapping ESR technology to quantify the formation of superoxide radicals (${}^{\bullet}O_2^-$) in the piezocatalytic system. As shown in Fig. 11(d), the ESR spectrum captures a characteristic 1 : 1 : 1 : 1 intensity ratio of the DMPO–${}^{\bullet}O_2^-$ adduct, confirming the presence of ${}^{\bullet}O_2^-$ radicals. This result strongly suggests that ${}^{\bullet}O_2^-$ is a crucial intermediate in the generation of H_2O_2.[57,58] As shown in the figure, the introduction of L-ascorbic acid (VC) significantly inhibits the generation of H_2O_2, providing strong evidence for the existence of superoxide radicals (${}^{\bullet}O_2^-$) as key intermediates in the reaction pathway. Based on these observations, we propose that the oxygen reduction reaction (ORR) proceeds *via* a two-step single-electron reduction mechanism (eqn (2) and (3)).[56]

In addition to the ORR pathway, we conducted active species capture experiments to validate the role of the water oxidation reaction (WOR) in the catalytic production of H_2O_2. As shown in the figure, the addition of *tert*-butanol (TBA), a scavenger for hydroxyl radicals (${}^{\bullet}OH$), also inhibited the formation of H_2O_2 in the piezocatalytic reaction system. This suggests that ${}^{\bullet}OH$ radicals play a significant role in the reaction pathway. Furthermore, as depicted in Fig. 11(b), the ESR spectrum revealed four characteristic peaks with an intensity ratio of 1 : 2 : 2 : 1, which are associated with ${}^{\bullet}OH$ radicals. This confirms the presence of ${}^{\bullet}OH$ in the system and supports the involvement of the WOR pathway in H_2O_2 generation. In Fig. 11(c), it is observed that the intensity of the TEMPO characteristic peak decreases significantly after the initiation of ultrasonication, indicating the formation of holes (h^+) in the heterojunction.[55] This provides direct evidence for the generation of h^+, which can participate in the water oxidation reaction (WOR) to produce H_2O_2. Various indications have also been shown that ${}^{\bullet}OH$ radicals can be used as a secondary source of H_2O_2 production (eqn (5)–(7)).[19] These findings confirm that the heterojunction can transform the generation of H_2O_2 from the single reaction pathway (*e.g.*, ORR alone) to the dual reaction pathway (ORR + WOR). The dual reaction pathway mechanism significantly enhances H_2O_2 production by leveraging both oxygen reduction and water oxidation processes, thereby improving the overall efficiency of the piezocatalytic system. This dual reaction pathway approach represents a major advancement in optimizing H_2O_2 generation for practical applications.

$$h^+ + OH^- \rightarrow {}^{\bullet}OH \quad (5)$$

$$ {}^{\bullet}OH + {}^{\bullet}OH \rightarrow H_2O_2 \quad (6)$$

$$h^+ + H_2O \rightarrow H_2O_2 + 2H^+ \quad (7)$$

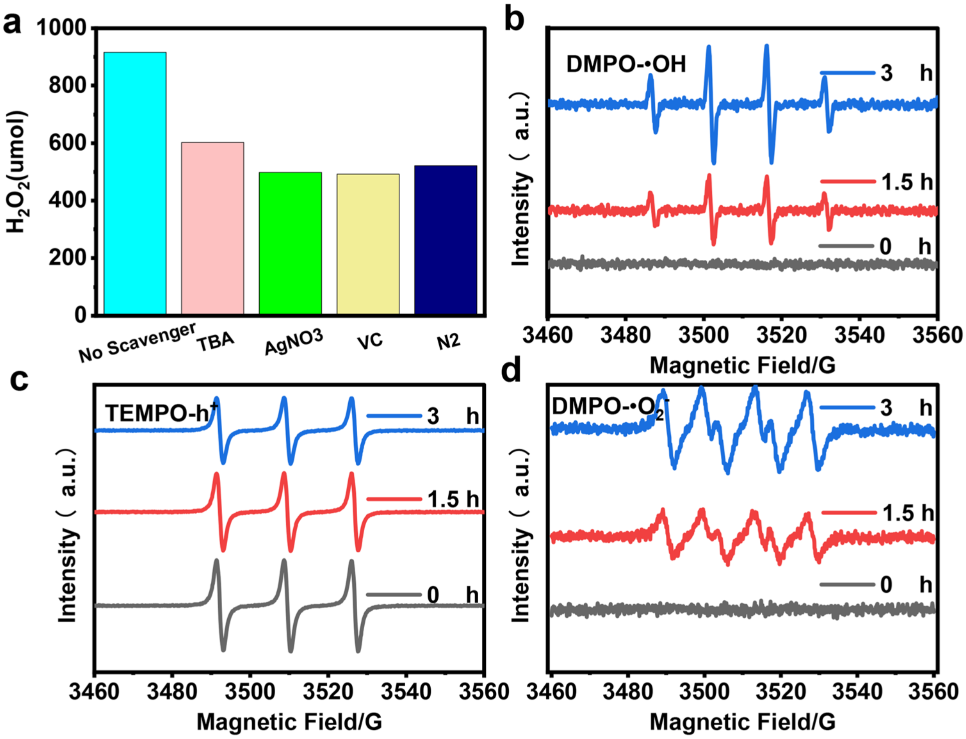

Fig. 11 (a) Quenching experiment of H_2O_2 production, (b) EPR spectra of •OH, (c) EPR spectra of h^+, and (d) EPR spectra of $•O_2^-$.

4. Conclusions

In summary, ZnO/Ag_2O S-type heterojunctions synthesized *via* a precipitation method exhibit superior performance compared to traditional type I or II heterojunctions. These S-type heterojunctions demonstrate enhanced charge separation efficiency, enabling more effective utilization of electrons and holes in the reaction process.[59] As a result, they achieve a significantly higher H_2O_2 yield of 346.9 μmol g^{-1} h^{-1} through piezoelectric catalysis, without compromising their redox capacity. This yield surpasses that of conventional photocatalysis and offers a greener and safer alternative to the traditional anthraquinone method. It is noteworthy that, in contrast to conventional catalytic systems relying on a single reaction pathway, this heterojunction catalyst exhibits a unique dual reaction pathway synergistic mechanism. As shown in Fig. 11(a), after adding ascorbic acid (VC) to scavenge superoxide radicals, the system still maintains a 51.7% H_2O_2 yield (excluding the contribution from the oxygen reduction pathway). This result demonstrates that the two reaction pathways contribute nearly equally (approaching a 1 : 1 ratio) to H_2O_2 generation, and such dual reaction pathway synergy significantly enhances the overall hydrogen peroxide production efficiency.

Conflicts of interest

The authors declare that they have no known competing financial interests or personal relationships that could have appeared to influence the work reported in this paper.

Data availability

Data are available at request from the authors.

Acknowledgements

This work was supported by National Natural Science Foundation, China (52162015), and Open Fund Projects of Sichuan Provincial University Key Laboratory of Green Catalysis, China (LZJ2004).

References

1 Y. Zhao, P. Zhang, Z. Yang, L. Li, J. Gao, S. Chen, T. Xie, C. Diao, S. Xi and B. Xiao, *et al.*, Mechanistic analysis of multiple processes controlling solar-driven H_2O_2 synthesis using engineered polymeric carbon nitride, *Nat. Commun.*, 2021, **12**(1), 3701.

2 Y. Wei, Y. Zhang, J. Miao, W. Geng and M. Long, *In situ* utilization of piezo-generated hydrogen peroxide for efficient *p*-chlorophenol degradation by Fe loading bismuth vanadate, *Appl. Surf. Sci.*, 2021, **543**, 148791.

3 F. Xue, Y. Si, M. Wang, M. Liu and L. Guo, Toward efficient photocatalytic pure water splitting for simultaneous H_2 and H_2O_2 production, *Nano Energy*, 2019, **62**, 823–831.

4 Y. Liu, Y. Chen, J. Deng and J. Wang, N-doped aluminum–graphite (Al–Gr–N) composite for enhancing *in situ*

production and activation of hydrogen peroxide to treat landfill leachate, *Appl. Catal., B*, 2021, **297**, 120407.

5 Y. Xia, X. Zhao, C. Xia, Z. Y. Wu, P. Zhu, J. Y. T. Kim, X. Bai, G. Gao, Y. Hu and J. Zhong, *et al.*, Highly active and selective oxygen reduction to H(2)O(2) on boron-doped carbon for high production rates, *Nat. Commun.*, 2021, **12**(1), 4225.

6 F. Sun, C. Yang, Z. Qu, W. Zhou, Y. Ding, J. Gao, G. Zhao, D. Xing and Y. Lu, Inexpensive activated coke electrocatalyst for high-efficiency hydrogen peroxide production: Coupling effects of amorphous carbon cluster and oxygen dopant, *Appl. Catal., B*, 2021, **286**, 119860.

7 X. Zhou, B. Shen, J. Zhai and J. C. Conesa, High Performance Generation of H(2)O(2) under Piezophototronic Effect with Multi-Layer In(2) S(3) Nanosheets Modified by Spherical ZnS and BaTiO(3) Nanopiezoelectrics, *Small Methods*, 2021, **5**(6), e2100269.

8 P. C. Sherrell, M. Fronzi, N. A. Shepelin, A. Corletto, D. A. Winkler, M. Ford, J. G. Shapter and A. V. Ellis, A bright future for engineering piezoelectric 2D crystals, *Chem. Soc. Rev.*, 2022, **51**(2), 650–671.

9 Y. Liu, S. Ye, H. Xie, J. Zhu, Q. Shi, N. Ta, R. Chen, Y. Gao, H. An and W. Nie, *et al.*, Internal-Field-Enhanced Charge Separation in a Single-Domain Ferroelectric $PbTiO_3$ Photocatalyst, *Adv. Mater.*, 2020, **32**(7), 1906513.

10 J. Wu, N. Qin, B. Yuan, E. Lin and D. Bao, Enhanced Pyroelectric Catalysis of BaTiO(3) Nanowires for Utilizing Waste Heat in Pollution Treatment, *ACS Appl. Mater. Interfaces*, 2018, **10**(44), 37963–37973.

11 K. Wang, C. Han, J. Li, J. Qiu, J. Sunarso and S. Liu, The Mechanism of Piezocatalysis: Energy Band Theory or Screening Charge Effect?, *Angew. Chem., Int. Ed.*, 2022, **61**(6), e202110429.

12 C. Wang, C. Hu, F. Chen, T. Ma, Y. Zhang and H. Huang, Design strategies and effect comparisons toward efficient piezocatalytic system, *Nano Energy*, 2023, **107**, 108093.

13 X. Shi, S. Back, T. M. Gill, S. Siahrostami and X. Zheng, Electrochemical Synthesis of H_2O_2 by Two-Electron Water Oxidation Reaction, *Chem*, 2021, **7**(1), 38–63.

14 C. Ling, D. Jin, R. Li, C. Li and W. Wang, Self-assembled membranes modulate the active site of carbon fiber paper to boost the two-electron water oxidation reaction, *Chem. Eng. J.*, 2023, **465**, 142903.

15 K. M. Lee, C. W. Lai, K. S. Ngai and J. C. Juan, Recent developments of zinc oxide based photocatalyst in water treatment technology: A review, *Water Res.*, 2016, **88**, 428–448.

16 W. E. Mahmoud, A. A. Al-Ghamdi, F. El-Tantawy and S. Al-Heniti, Synthesis, characterization and charge transport mechanism of CdZnO nanorods, *J. Alloys Compd.*, 2009, **485**(1–2), 59–63.

17 A. Kadam, R. Dhabbe, A. Gophane, T. Sathe and K. Garadkar, Template free synthesis of ZnO/Ag_2O nanocomposites as a highly efficient visible active photocatalyst for detoxification of methyl orange, *J. Photochem. Photobiol., B*, 2016, **154**, 24–33.

18 L. Meng, C. Zhao, X. Zhang, R. Guo, Y. Zheng, H. Chu, H. Fu, P. Wang and C.-C. Wang, Piezo-photocatalytic synergetic for H_2O_2 generation *via* dual-pathway over *Z*-scheme ZIF-L/g-C_3N_4 heterojunction, *Nano Energy*, 2024, **128**, 109795.

19 C. Zhao, Y. Li, H. Chu, X. Pan, L. Ling, P. Wang, H. Fu, C. C. Wang and Z. Wang, Construction of direct *Z*-scheme Bi(5)O(7)I/UiO-66-NH(2) heterojunction photocatalysts for enhanced degradation of ciprofloxacin: Mechanism insight, pathway analysis and toxicity evaluation, *J. Hazard. Mater.*, 2021, **419**, 126466.

20 L. Wang, J. Zhang, Y. Zhang, H. Yu, Y. Qu and J. Yu, Inorganic Metal-Oxide Photocatalyst for H_2O_2 Production, *Small*, 2021, **18**(8), 2104561.

21 H. Zhang, Y. H. Sun, S. L. An, R. H. Guo, R. F. Wang and Y. W. Ma, Construction of CeCux-BTC/CN S-type heterojunctions and photocatalytic CO_2 reduction to CO and CH_4, *RSC Adv.*, 2025, **15**(11), 8541–8552.

22 K. Meng, J. Zhang, B. Zhu, C. Jiang, H. García and J. Yu, Interfacial Charge Transfer in ZnO/COF S-Scheme Photocatalyst *via* Zn–N Bond, *Adv. Mater.*, 2025, 2505088.

23 Y. Ma, D. He, Q. Liu, S. Le, X. Wang and A. S-type, 2D/2D heterojunction *via* intercalating ultrathin g-C_3N_4 into $NH_4V_4O_{10}$ nanosheets and the boosted removal of ciprofloxacin, *Appl. Catal., B*, 2024, 344.

24 W. Fu, M. Yu, M. Yang, H. Yu, Y. Yang, S. Qian, X. Dong and L. Xia, Preparation of Pumice Stone Morphology $AgAlO_2$@ZnO S-Type Heterojunction Photocatalyst with the Synergistic Effect of Photocatalytic Degradation and Hydrogen Production, *Cryst. Growth Des.*, 2023, **23**(4), 2331–2342.

25 H. Li, W. Ma, X. Zeng, S. Liu, L. Xiao, Z. Fang, Y. Feng, M. Yang, H. Zhu and Y. Yang, *et al.*, ZnO/CuO Piezoelectric Nanocatalysts for the Degradation of Organic Pollutants, *ACS Appl. Nano Mater.*, 2023, **6**(22), 21113–21122.

26 Z. Yang, C. Deng, Y. Ding, H. Luo, J. Yin, Y. Jiang, P. Zhang and Y. Jiang, Eco-friendly and effective strategy to synthesize ZnO/Ag_2O heterostructures and its excellent photocatalytic property under visible light, *J. Solid State Chem.*, 2018, **268**, 83–93.

27 Y. Liu, S. Wei and W. Gao, Ag/ZnO heterostructures and their photocatalytic activity under visible light: effect of reducing medium, *J. Hazard. Mater.*, 2015, **287**, 59–68.

28 Z. Shen, X. Zhang, R. Mi, M. Liu, Y. Chen, C. Chen and S. Ruan, On the high response towards TEA of gas sensors based on Ag-loaded 3D porous ZnO microspheres, *Sens. Actuators, B*, 2018, **270**, 492–499.

29 Z. Wang, A. Ali Haidry, L. Xie, A. Zavabeti, Z. Li, W. Yin, R. Lontio Fomekong and B. Saruhan, Acetone sensing applications of Ag modified TiO_2 porous nanoparticles synthesized *via* facile hydrothermal method, *Appl. Surf. Sci.*, 2020, **533**, 147383.

30 X.-Y. Xie, L.-Y. Li, P. Zhan, M. Liang, S.-M. Xie, J.-X. Meng, Y. Bai and W.-J. Zheng, Fast one-step synthesis of ZnO submicrospheres in PEG200, *J. Mater. Sci.*, 2013, **49**(5), 2355–2361.

31 M. P. Gaigeot, Theoretical spectroscopy of floppy peptides at room temperature. A DFTMD perspective: gas and aqueous phase, *Phys. Chem. Chem. Phys.*, 2010, **12**(14), 3336–3359.

32 L. Ohlin, P. Bazin, F. Thibault-Starzyk, J. Hedlund and M. Grahn, Adsorption of CO_2, CH_4, and H_2O in Zeolite

ZSM-5 Studied Using *In Situ* ATR-FTIR Spectroscopy, *J. Phys. Chem. C*, 2013, **117**(33), 16972–16982.

33 Y. Cui, J. Briscoe and S. Dunn, Effect of Ferroelectricity on Solar-Light-Driven Photocatalytic Activity of $BaTiO_3$—Influence on the Carrier Separation and Stern Layer Formation, *Chem. Mater.*, 2013, **25**(21), 4215–4223.

34 Y. Cai, Y. Zhang, Z. Lv, S. Zhang, F. Gao, M. Fang, M. Kong, P. Liu, X. Tan and B. Hu, *et al.*, Highly efficient uranium extraction by a piezo catalytic reduction-oxidation process, *Appl. Catal., B*, 2022, **310**, 121343.

35 S. Lin, S. Li, H. Huang, H. Yu and Y. Zhang, Synergetic Piezo-Photocatalytic Hydrogen Evolution on Cd(x) Zn($1-x$) S Solid-Solution 1D Nanorods, *Small*, 2022, **18**(8), e2106420.

36 Y. Zhang, L. Wang, H. Huang, C. Hu, X. Zhang, C. Wang and Y. Zhang, Water flow induced piezoelectric polarization and sulfur vacancy boosting photocatalytic hydrogen peroxide evolution of cadmium sulfide nanorods, *Appl. Catal., B*, 2023, **331**, 122714.

37 S. Lin, Q. Wang, H. Huang and Y. Zhang, Piezocatalytic and Photocatalytic Hydrogen Peroxide Evolution of Sulfide Solid Solution Nano-Branches from Pure Water and Air, *Small*, 2022, **18**(19), e2200914.

38 C. Wang, F. Chen, C. Hu, T. Ma, Y. Zhang and H. Huang, Efficient piezocatalytic H_2O_2 production of atomic-level thickness $Bi_4Ti_3O_{12}$ nanosheets with surface oxygen vacancy, *Chem. Eng. J.*, 2022, **431**, 133930.

39 K. Wang, J. Li, X. Liu, Q. Cheng, Y. Du, D. Li, G. Wang and B. Liu, Sacrificial-agent-free artificial photosynthesis of hydrogen peroxide over step-scheme WO_3/NiS hybrid nanofibers, *Appl. Catal., B*, 2024, **342**, 123349.

40 Y. Son and J. Seo, Effects of gas saturation and sparging on sonochemical oxidation activity in open and closed systems, Part I: H_2O_2 generation, *Ultrason. Sonochem.*, 2022, **90**, 106214.

41 N. Wang, R.-X. Wang, Z.-J. Li, R. Liu, H. Gao, H.-Y. Chen, R. Li, Y.-Z. Long and H.-D. Zhang, $NiFe_2O_4$ Nanofibers with Surface Oxygen Vacancies for Piezo-Catalytic Hydrogen Peroxide Production, *ACS Appl. Nano Mater.*, 2023, **6**(16), 15063–15072.

42 X. Liu, M. Wang, Y. Li, X. Li, J. Zhang, S. Yang, J. Wu, L. Wang, J. Li and F. Li, Bismuth titanate microplates with tunable oxygen vacancies for piezocatalytic hydrogen peroxide production, *J. Colloid Interface Sci.*, 2025, **678**(Pt B), 246–255.

43 N. Alhokbany, T. Ahamad and S. M. Alshehri, Fabrication of highly porous ZnO/Ag_2O nanoparticles embedded in N-doped graphitic carbon for photocatalytic degradation of tetracycline, *J. Environ. Chem. Eng.*, 2022, **10**(3), 107681.

44 D. Shao, L. Zhang, S. Sun and W. Wang, Oxygen Reduction Reaction for Generating H(2) O(2) through a Piezo-Catalytic Process over Bismuth Oxychloride, *ChemSusChem*, 2018, **11**(3), 527–531.

45 Y. Li, L. Li, F. Liu, B. Wang, F. Gao, C. Liu, J. Fang, F. Huang, Z. Lin and M. Wang, Robust route to H_2O_2 and H_2 *via* intermediate water splitting enabled by capitalizing on minimum vanadium-doped piezocatalysts, *Nano Res.*, 2022, **15**(9), 7986–7993.

46 K. Wang, D. Shao, L. Zhang, Y. Zhou, H. Wang and W. Wang, Efficient piezo-catalytic hydrogen peroxide production from water and oxygen over graphitic carbon nitride, *J. Mater. Chem. A*, 2019, **7**(35), 20383–20389.

47 P. Wang, X. Li, S. Fan, X. Chen, M. Qin, D. Long, M. O. Tadé and S. Liu, Impact of oxygen vacancy occupancy on piezocatalytic activity of $BaTiO_3$ nanobelt, *Appl. Catal., B*, 2020, **279**, 119340.

48 Y. Ma, B. Wang, Y. Zhong, Z. Gao, H. Song, Y. Zeng, X. Wang, F. Huang, M.-R. Li and M. Wang, Bifunctional $RbBiNb_2O_7$/poly(tetrafluoroethylene) for high-efficiency piezocatalytic hydrogen and hydrogen peroxide production from pure water, *Chem. Eng. J.*, 2022, **446**, 136958.

49 H. Zhang, L. Jia, P. Wu, R. Xu, J. He and W. Jiang, Improved H_2O_2 photogeneration by KOH-doped g-C_3N_4 under visible light irradiation due to synergistic effect of N defects and K modification, *Appl. Surf. Sci.*, 2020, **527**, 146584.

50 H. P. Toan, D.-V. Nguyen, P. D. M. Phan, N. H. Anh, P. P. Ly, M.-T. Pham, S. H. Hur, T. D. T. Ung, D. D. Bich and H.-T. Vuong, Simultaneously Utilizing Excited Holes and Electrons for Piezoelectric-Enhanced Photoproduction of H_2O_2 from S-Scheme 2D S-doped VO_x/g-C_3N_4 Nanostructures, *ACS Appl. Mater. Interfaces*, 2024, **16**(22), 29421–29438.

51 R. Wang, K. Pan, D. Han, J. Jiang, C. Xiang, Z. Huang, L. Zhang and X. Xiang, Solar-Driven H_2O_2 Generation From H_2O and O_2 Using Earth-Abundant Mixed-Metal Oxide@ Carbon Nitride Photocatalysts, *ChemSusChem*, 2016, **9**(17), 2470–2479.

52 G. Yin, C. Fu, F. Zhang, T. Wu, S. Hao, C. Wang and Q. Song, Piezocatalytic degradation of organic dyes and production of H_2O_2 with hydroxyapatite, *J. Alloys Compd.*, 2023, **937**, 168382.

53 F. N. Habarugira, D. Yao, W. Miao, C. Chu, Z. Chen and S. Mao, Synergy of sodium doping and nitrogen defects in carbon nitride for promoted photocatalytic synthesis of hydrogen peroxide, *Chin. Chem. Lett.*, 2024, **35**(8), 109886.

54 R. M. Mohamed, A. A. Ismail, M. W. Kadi, A. S. Alresheedi and I. A. Mkhalid, Facile Synthesis of Mesoporous Ag_2O–ZnO Heterojunctions for Efficient Promotion of Visible Light Photodegradation of Tetracycline, *ACS Omega*, 2020, **5**(51), 33269–33279.

55 Y. Cui, F. Wang, P. Yuan, W. Liu, B. Fang, Z. Wang and Y. Pu, Harvesting Vibration Energy to Produce Hydrogen Peroxide with Bi_3TiNbO_9 Nanosheets through a Water Oxidation Dominated Dual-Channel Pathway, *ACS Sustainable Chem. Eng.*, 2024, **12**(9), 3595–3607.

56 Z. Wei, S. Zhao, W. Li, X. Zhao, C. Chen, D. L. Phillips, Y. Zhu and W. Choi, Artificial Photosynthesis of H_2O_2 through Reversible Photoredox Transformation between Catechol and *o*-Benzoquinone on Polydopamine-Coated CdS, *ACS Catal.*, 2022, **12**(18), 11436–11443.

57 L. Fang, K. Wang, C. Han, X. Li, P. Li, J. Qiu and S. Liu, Comparative investigation of piezocatalysts composed of

La, Sr and Co (Fe) complex oxides in Ruddlesden–Popper type or simple single perovskites for efficient hydrogen peroxide generation, *Chem. Eng. J.*, 2023, **461**, 141866.

58 K. Wang, M. Zhang, D. Li, L. Liu, Z. Shao, X. Li, H. Arandiyan and S. Liu, Ternary BaCaZrTi perovskite oxide piezocatalysts dancing for efficient hydrogen peroxide generation, *Nano Energy*, 2022, **98**, 107251.

59 W. Fang and L. Wang, S-Scheme Heterojunction Photocatalyst for Photocatalytic H_2O_2 Production: A Review, *Catalysts*, 2023, **13**(10), 1325.